Materials Transactions, Vol. 47, No. 11 (2006) pp. 2745 to 2752
Special Issue on Advances in Computational Materials Science and Engineering IV

Finite Element Simulation of Liquid Phase Sintering with Tungsten Heavy Alloys

Seong Jin Park[1], Suk Hwan Chung[2], John L. Johnson[3] and Randall M. German[1]

[1]*Center for Advanced Vehicular Systems, PO Box 5405, Mississippi State University, Mississippi State, MS 39762, USA*
[2]*CetaTech, Inc., TIC, 296-3, Seonjin-ri, Yonghyeon-myon, Sacheon, Kyongnam, 664-953, S. Korea*
[3]*Breakthrough Technology, Kennametal, Inc., 1600 Technology Way, Latrobe, PA 15650, USA*

Densification and distortion of W-Ni-Fe tungsten heavy alloys during liquid phase sintering are modeled using constitutive laws of grain growth, densification, and deformation. The models are "calibrated" via carefully designed experiments to obtain the necessary parameters to enable modeling. Metallographic analysis of quenched samples is used to obtain grain size data as functions of time and temperature, while dilatometry and dimensional analyses are used to determine the bulk viscosity and shear viscosity. The influences of gravity, substrate friction, surface tension, and solid content on distorted shapes are shown by comparing predictions from the finite element method with experimentally measured shapes. The finite element simulations accurately predict several phenomena, including increased distortion with longer sintering times and higher liquid contents, slumping due to gravity, spheroidization due to surface tension, and friction-related distortion due to sticking of the part to the substrate. [doi:10.2320/matertrans.47.2745]

(Received May 22, 2006; Accepted August 2, 2006; Published November 15, 2006)

Keywords: *distortion, finite element method, liquid phase sintering, modeling, tungsten heavy alloy*

1. Introduction

Particulate materials processing routes consist of a variety of near-net shaping techniques. Various shaping methods such a compaction, injection molding, tape casting, and more recently rapid prototyping have been developed and advanced through the last several decades. Irrespective of the shaping process used, densification and strengthening of a green body depends on the sintering process. Sintering processes can be enhanced by additives that form a high diffusivity second phase, which may be solid or liquid. Liquid phase sintering (LPS) can provide especially rapid densification and homogenization. In spite of the benefits of using a liquid phase for high-performance and low-cost manufacturing, most liquid phase sintered compositions are relatively low in liquid content due to distortion concerns. An understanding of the distortion phenomena and the factors governing such behavior is important to realize novel microstructures and properties.

In the past few years continuum modeling has gained relevance in this aspect via the efforts of Ashby,[1] McMeeking & Kuhn,[2] Olevsky *et al.*,[3] Riedel *et al.*,[4] McHugh and Riedel,[5] Bouvard and Meister,[6] Cocks,[7] and Bordia and Schrerer.[8] Modeling efforts based on constitutive laws of deformation offer insights to the scientific community and are capable of providing solutions and in-line monitoring tools for manufacturers. The deformation behavior of a porous material during densification is approximated by assuming that material behaves as a linear viscous incompressible body with the elimination of pores during densification under the application of external force during hot isostatic pressing or due to the sintering stress during free sintering.

In the above mentioned studies, the focus was on the prediction of densification during solid state sintering. The effects due to gravity, friction, and surface tension are relatively small compared to those of inherent sintering stresses in systems dominated with solid-state sintering events and are usually neglected. Further, the above-mentioned studies overlook grain growth during sintering which generally leads to an overestimation of the sintering stresses in the late stages of sintering. However, such factors cannot be ignored in considering the densification and distortion issues during liquid phase sintering, especially since grain growth is often very rapid once the liquid forms.

Experiments by Lenel *et al.*[9] on copper and Upadhyaya and German[10] on tungsten heavy alloys (WHAs) illustrate the importance of gravity and friction on the densification and distortion behavior during sintering. Raman and German[11] considered the influence of gravity on the distortion of tungsten heavy alloys and proposed a rheological model to predict the shape. Ganesan *et al.*[12] and Binet *et al.*[13] considered a densified LPS component to be a viscous mass and modeled distortion behavior using Navier-Stokes equations. Olevsky *et al.*[3] considered the effect of gravity and friction on distortion assuming that the material obeys power law creep behavior under uniaxial loading. However, in liquid phase sintering the effect of surface tension as well as gravity and friction should be included to give better predictions of actual distortion behavior.

In this study, we present our efforts at predicting the phenomena of grain growth, densification, and distortion using a finite element model (FEM) which utilizes constitutive equations applicable to a linear viscous compressive material. The model is used to predict the final shape of sintered W-Ni-Fe components with consideration of grain growth, gravity, friction, surface tension, and solid content during sintering. The relative influence of these parameters on the distortion behavior is also examined.

2. Experimental

2.1 Powder and Sample Preparation

The characteristics of the as-received W, Ni, and Fe

Table 1 Powder characteristics and tungsten heavy alloy compositions.

element		W	Ni	Fe
vendor		Osram	Novamet	ISP
designation		M-37	123	CIP-R1470
fabrication method		oxide reduction	carbonyl process	carbonyl process
powder properties	D_{10} (μm)	2	3	2
	D_{50} (μm)	6	10	6
	D_{90} (μm)	10	24	10
	apparent density (kg/m^3)	4100 (21%)	2300 (26%)	2400 (31%)
	tap density (kg/m^3)	6200 (32%)	3300 (37%)	4600 (59%)
	pycnometer density (kg/m^3)	19200	8960	7890
	BET surface area (m^2/g)	0.18	0.60	0.45
	Melting Point (°C)	3410	1455	1535
78% WHA	mass%	78.0	15.4	6.6
	volume %	61.4	26.0	12.6
	density (kg/m^3)		15110	
83% WHA	mass%	83.0	11.9	5.1
	volume %	68.5	21.2	10.3
	density (kg/m^3)		15940	
88% WHA	mass%	88.0	8.4	3.6
	volume %	76.6	15.7	7.7
	density (kg/m^3)		16800	
93% WHA	mass%	93.0	4.9	2.1
	volume %	85.6	9.7	4.7
	density (kg/m^3)		17760	

powders selected for this study are given in Table 1. The tungsten powder used in the mixture was rod milled to deagglomerate the as-received powder. The rod milling operation was performed dry for 1 hour in a 2000 cm^3 capacity plastic jar at 90 rpm using greater than 95% pure tungsten rods with a diameter of 10 and 180 mm in length. The weight ratio of rods to powder was 10 : 1 with the volume of the milling rods being approximately 40% of the jar volume. The milling jar was evacuated, argon back filled, and tape sealed in order to prevent oxidation.

Elemental W, Ni, and Fe powders were weighted accurately to make up the desired compositions. All experiments were conducted on 78, 83, 88 and 93 W with the balance being Ni and Fe in the ratio of 7 : 3. The weighed powders were subsequently placed in a 500 cm^3 capacity plastic jar and mixed in a Turbula mixer (model: T2C, supplier: Glen Mills) for 30 minutes. The homogenously mixed powders were compacted uniaxially into cylinders of 12.7 mm in diameter and 10.0 mm in height using a Carver press at a pressure of 175 MPa. The green densities of all samples for both dilatometry and quenching were 60% of theoretical.

2.2 Quenching Test

Quenching experiments were conducted to obtain data for grain growth. The samples were placed in a molybdenum crucible suspended in the hot zone of a vertical CM furnace with a tungsten wire. Sintering was performed in a dry H_2 atmosphere. The samples were heated at 10°C/min up to 900°C with a 1 hour hold to reduce oxides on the powders. Next, the temperature was increased at 5°C/min until the target temperature for quenching, where the samples were held for various times between 0 and 60 min. The special design of the furnace allowed the sintered compacts to be quenched in water to obtain the instantaneous microstructure at the desired temperatures and times.

The quenched samples were sectioned top-to-bottom and mounted using epoxy resin under vacuum to fill the porosity and to prevent the smearing of the material into the pores. The polishing procedure involved the use of a 9 μm diamond suspension followed by 6, 3, and 1 μm diamond suspensions on a MD-DAC cloth from Struers. A mirror-like finish was obtained by giving a final polish with a 0.04 μm silica colloidal suspension (OP-S from Struers). Next, the microstructure was revealed by chemically etching with a solution of 6 g of potassium ferricyanate and 0.5 g of potassium hydroxide in 50 ml of distilled water. The microstructure was imaged using scanning electron microscopy (SEM; TopCon Model ABT-32, Tokyo, Japan). An analysis routine was developed to measure the W grain size on the polishing plane using Clemex (Longueuil, Canada) Version PE 3.5 software. The size of each W grain was represented as the diameter of a circle with the same area. Five different fields and a minimum of 400 grains per sample were used for each average grain size measurement. The starting grain size G_0 was determined by mounting the milled W powder in epoxy, polishing to reveal grain cross-sections, and determining the average size using the same image analysis procedure as for the quenched samples.

2.3 Dilatometry Test

In order to obtain material parameters for densification, dilatometry experiments were conducted on all compositions for *in situ* measurement of shrinkage, shrinkage rate, and the temperature at which phase changes happen. The experiments were performed using a vertical push rod dilatometer in hydrogen (ANTER Unitherm™ Model 1161) with three different heating rates both in solid state and liquid phase sintering. The dilatometer was also used to measure the thermal expansion of each composition during a controlled cool down at a rate of 10°C/min from the sintering temperature.

2.4 Distortion Test

Cylindrical samples were pre-sintered for 1 hour at 1000°C. We used two different sintering temperatures (1500 and 1530°C) and two different holding times (30 and 60 min) for each sintering temperature. The heating and cooling rate was fixed to 10°C/min when the sample was heated up to the sintering temperature and cooled down to room temperature.

3. Governing Equations of Sintering

Methodologies to model sintering are classified into continuum, micromechanical, multi-particle, and molecular dynamics models on the basis of length scales.[14] Among these methodologies, continuum models have benefits in terms of computing time and macroscopic concerns of shape prediction. For this continuum approach, firstly mass conservation is evoked via the following equation:

$$\frac{\dot{\rho}}{\rho} = -\dot{\varepsilon}_{kk} \tag{1}$$

where ρ is the relative (fractional) density, $\dot{\rho}$ is the time derivative of ρ, and $\dot{\varepsilon}_{kk}$ is the first invariant of the true strain rate $\dot{\varepsilon}_{ij} = (\dot{u}_{i,j} + \dot{u}_{j,i})/2$ with displacement vector u_i and its time derivative $\dot{u}_i$. This equation expresses densification behavior during sintering.

The second governing equation is momentum conservation, which requires force-stress equilibrium:

$$\sigma_{ij,j} + f_i = 0 \tag{2}$$

where σ_{ij} is the true stress and f_i is the body force defined as follows:

$$f_i = \begin{cases} -\rho\rho_t g & \text{in the vertical direction} \\ 0 & \text{otherwise} \end{cases} \tag{3}$$

where ρ_t is the theoretical density and g the gravitational acceleration. Gravitational force may generate heterogeneous deformation, since it is unidirectional. The influence of gravity is treated in the above equations under various gravitational environments.

Following McMeeking & Kuhn,[2] the deformation rate (true strain rate) $\dot{\varepsilon}_{ij}$ of the porous compact is expressed as:

$$\dot{\varepsilon}_{ij} = \frac{1}{2\eta}\sigma'_{ij} + \frac{1}{3K}(\sigma_m - \sigma_s)\delta_{ij} \tag{4}$$

where, σ'_{ij} and σ_m are the deviatoric and hydrostatic ($\sigma_{kk}/3$) parts of the true stress σ_{ij}, δ_{ij} is the Kronecker delta, σ_s is the sintering stress, η is the effective shear viscosity, and K is the effective bulk viscosity of porous powder compacts. The formulations for sintering stress and the bulk viscosity are detailed by Kwon *et al.*[15] and are adapted here for activated and liquid phase sintering. In the finite element simulation, eq. (4) is solved simultaneously with eq. (2), which uses the $\sigma_{ij,j}$ terms. It is noted that uniform temperature is imposed in part based on the sintering cycle.

3.1 Sintering stress

The sintering stress σ_s is the driving force for densification due to interfacial energy of pores and grain boundaries and varies with the nature and extent of relative density (ρ) and porosity ($\theta = 1 - \rho$). Following Ashby[1] and Kwon *et al.*,[15] the sintering process is divided into different stages based on the density of the tungsten skeleton ρ_W. The initial stage, where $\rho_W \leq 0.85$, is characterized by an interconnected matrix phase (Ni-Fe) with porosity. The final stage with $\rho_W \geq 0.95$, is characterized by a closed matrix phase (Ni-Fe) with porosity. A combination of open and closed porosity exists in the intermediate stage where $0.85 < \rho_W < 0.95$. The sintering stresses during these stages are given as:

$$\sigma_s = \frac{6\gamma}{G}\frac{\rho^2(2\rho - \rho_0)}{\theta_0} \quad \text{for } \rho_W < 0.85, \tag{5}$$

$$\sigma_s = \frac{2\gamma}{G}\left(\frac{6\rho}{\theta}\right)^{1/3} \quad \text{for } \rho_W > 0.95, \text{ and} \tag{6}$$

$$\sigma_s = \frac{(\rho_2 - \rho)}{(\rho_2 - \rho_1)}\sigma_{si} + \frac{(\rho - \rho_1)}{(\rho_2 - \rho_1)}\sigma_{sf} \quad \text{for } 0.85 \leq \rho_W \leq 0.95 \tag{7}$$

where γ is the surface energy, G is the grain size, ρ_0 is the initial relative density of tungsten skeleton, θ_0 is the initial porosity of tungsten skeleton, ρ_1 is 0.85, ρ_2 is 0.95, and σ_{si} and σ_{sf} are the initial and final stage sintering stresses at $\rho_W = \rho_1$ and ρ_2, respectively.

3.2 Bulk viscosity

An expression for bulk viscosity is obtained by considering a single dominant densification mechanism. Assuming grain boundary diffusion through a segregated, high diffusivity second phase to be the dominant mechanism, the effective bulk viscosity is given by Kwon *et al.*[16] as follows:

$$K_i = \frac{\rho(\rho - \rho_0)^2}{3\theta_0^2}\frac{TG^3}{\mathrm{A}_i} \quad \text{for } \rho \leq 0.92 \tag{8}$$

$$K_f = \frac{\rho}{3\theta_0^{1/2}}\frac{TG^3}{\mathrm{A}_f} \quad \text{for } \rho \geq 0.92 \tag{9}$$

where T is the temperature and A_i and A_f are the effective material parameters in the initial and final regions of sintering, respectively. These effective material parameters A_i and A_f can be expressed as:

$$\mathrm{A}_i(T) = \frac{3C_i\Omega\delta D_b}{k} = \alpha_i \exp(-Q_b/RT) \tag{10}$$

$$\mathrm{A}_f(T) = \frac{3C_f\Omega\delta D_b}{k} = \alpha_f \exp(-Q_b/RT) \tag{11}$$

where k is the Boltzman's constant, Ω is the atomic volume, δ is the grain boundary thickness, D_b is the diffusion coefficient of W in the second phase, Q_b is the activation energy, and C_i, C_f, α_i, and α_f are material constants. Imposing the condition that eqs. (10) and (11) are equal at $\rho = 0.92$, the relationship between α_i and α_f is obtained as:

$$\alpha_f = \frac{\theta_0^2}{\sqrt{0.08}(0.92 - \rho_0)^2}\alpha_i \tag{12}$$

Since sintering behavior abruptly varies before and after liquid formation and in general liquid forms after all the pores close, material parameters for α_f need to divided into two cases, before liquid formation and after liquid formation. Therefore, the expression for the effective material parameter α_f is modified for liquid phase sintering as follows:

$$\mathrm{A}_f(T) = \alpha_{fs}\exp(-Q_{bs}/RT) \quad \text{before liquid formation} \tag{13}$$

$$\mathrm{A}_f(T) = \alpha_{fl}\exp(-Q_{bl}/RT) \quad \text{after liquid formation} \tag{14}$$

where Q_{bs} and Q_{bl} are activation energies in solid state and liquid phase and α_{fs}, and α_{fl} are material constants in the solid state and liquid phase, respectively. These parameters are determined from dilatometry experimental data based on the master sintering curve concept.[17]

3.3 Shear viscosity

During the sintering of tungsten heavy alloys, particle and neck dissolution ensues immediately after liquid formation, followed by rearrangement and grain growth. Near full density (96 to 98% depending on the tungsten content) is achieved prior to liquid formation and grain rearrangement does not significantly affect our assumption of densification predominantly due to grain boundary diffusion. Neck dissolution results in a decrease in the coordination number–leading to soft shear modes as suggested by Riedel *et al.*,[4] which is generally not observed for solid state sintering systems or LPS systems with very high solid content due to high contiguity and connectivity, providing the necessary resistance to deformation. Hence, prior to liquid formation, shear viscosity, expressed in a form very similar to the bulk viscosity, can be approximated by assuming $\eta/K = 0.6$ as suggested by the analysis of Riedel *et al.*[4] However, there are considerable conceptual and experimental difficulties that we encountered in using a shear viscosity of the form given in eqs. (8) and (9).

For this study, the rheological model proposed by Raman and German[10] is used to model the deformation behavior after densification. The shear viscosity of the liquid-solid system expressed as a function of the volume fraction of solid and viscosity of the liquid matrix phase, temperature, grain size, and the volume fraction of solid phase is given as:

$$\eta = \eta_l \left(\frac{G}{G_0}\right)^2 \frac{\beta \exp(-Q_d/RT)}{(1-\phi/\phi_c)^m} \tag{15}$$

where η_l is the Newtonian constant viscosity of the liquid matrix phase, G_0 is the initial grain size, Q_d is the activation energy for distortion, ϕ is the volume fraction of the solid phase, ϕ_c is the critical value for the liquid-solid system, β is a material constant, and $1 \leq m \leq 2$. Raman and German[10] found that the critical value ϕ_c for W-Ni-Fe system is 0.830 and the volume fraction of the solid phase ϕ for 88W-8.4Ni-3.6Fe is 0.765.

For the given sintering system, with assumption of perfect homogeneity, which means ϕ is constant, eq. (15) can be simplified as:

$$\eta = \beta_d \left(\frac{G}{G_0}\right)^2 \exp(-Q_d/RT) \tag{16}$$

where β_d is a material constant. Parameters Q_d and β_d are determined from distortion experimental data.

3.4 Grain growth

Though grain size significantly influences sintering behavior, grain growth has been sometimes neglected in modeling sintering behavior. To precisely model sintering behavior, bulk and shear viscosities used in this paper are also given as the function of grain size as shown above. The grain growth rate for coarsening of solid particles dispersed within a matrix phase according to Greenwood[18] is given by:

$$\frac{dG}{dt} = \frac{k'}{G^2} \tag{17}$$

where t represents the time and k' is a temperature dependent material parameter, expressed as follows:

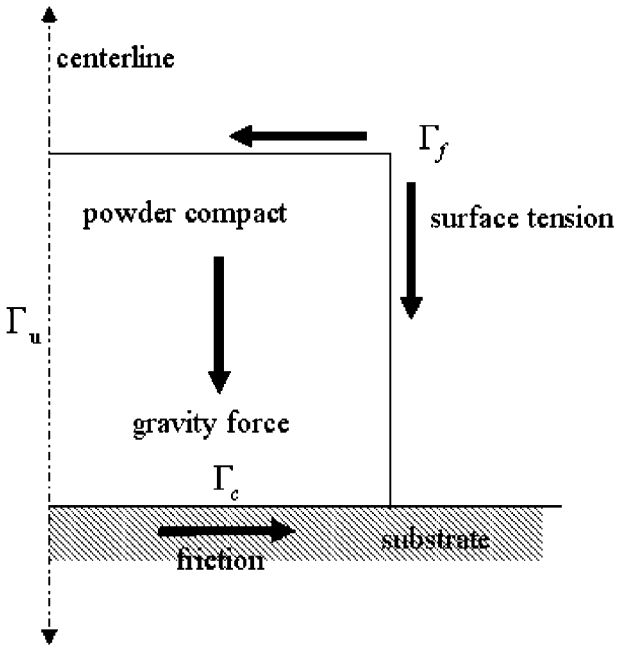

Fig. 1 Description of boundaries and acting forces.

$$k' = k_0 \exp(-Q_G/RT) \tag{18}$$

where k_0 and Q_G are a material constant and the activation energy for grain growth, respectively. Equation (17) was originally derived and assumed to be valid for spherical grains with no interaction between the diffusion fields of individual grains. Experimental data compiled by Lu and German[19] and simulation results, for example the work of Tikare and Cawley,[20] suggest that eq. (17) is valid for high solid concentrations. In the present study, the activation energy, Q_G, and the material constant, k_0, are obtained from quenching experimental data. Similarly to modeling of viscosities, two parameters k_0 and Q_G are divided into two periods of before (k_{0s} and Q_{Gs}) and after (k_{0l} and Q_{Gl}) liquid formation. These parameters are determined from experimental data based on the master sintering curve concept.[21]

4. Initial and Boundary Conditions

To solve the differential governing equation with the models described in the previous section, initial and boundary conditions are needed. The initial relative density and initial grain size should be considered as input conditions. The three different boundaries should be considered, as shown in Fig. 1; $\Gamma_\mathbf{u}$ is a velocity prescribed boundary, where the radial directional velocity in the axisymmetric plane is set to 0, Γ_c is a substrate-contacted boundary, and Γ_f is a free surface. Powder compacts can distort during sintering due to friction and surface tension effects as well as gravity, even if the density distribution after the shaping process is uniform. These two factors can be considered as described in the following sections.

4.1 Friction effect

When the solid-solid bonds become weak due to an increase in temperature, the friction between powder com-

pact and supporting plate is no longer negligible. To model the friction effect Coulomb friction is adopted as follows.

$$\sigma_t = \mu\sigma_n \tag{19}$$

where σ_t is the tangential frictional stress along the substrate and sample interface, σ_n is the normal stress, and μ is the Coulomb frictional coefficient. Equation (19) is applied as a boundary condition in the FEM simulation. The friction coefficient should change before and after liquid formation because powder compacts with large amounts of liquid adhere to the substrate. However, in this study a constant frictional coefficient of 0.3 is used for simplicity.

4.2 Surface tension effect

At the surface of different fluids, such as that between a liquid and a gas, uneven molecular forces at the free surface cause surface tension. Jagota and Dawson[22] simulated the viscous sintering of two particles in response to surface tension and Navti *et al.*[23] modeled surface tension effects in mold filling problems. According to those studies, the normal stress induced by the surface tension on the free surface boundary Γ_f is written below.

$$\sigma_n = \gamma\kappa \quad \text{on} \quad \Gamma_f \tag{20}$$

where κ is the mean curvature of the free surface defined as follows.

$$\kappa = -\nabla \cdot \mathbf{n} \tag{21}$$

where $\mathbf{n}$ is the outward unit normal on the surface. Equation (20) is applied as a free surface boundary condition in the simulation.

5. Finite Element Formulation

We derived the following integral statement equivalent to the above boundary value problem:

Among the velocity fields $\dot{u}_i$ satisfying the velocity prescribed boundary conditions, find $\dot{u}_i$, which satisfies the following variational equation for arbitrary functions ω_i that vanish on $\Gamma_{\mathbf{u}}$.

$$\int_\Omega 2\mu\dot{\varepsilon}'_{ij}\omega'_{ij}d\Omega + \int_\Omega (K\dot{\varepsilon}_{kk} + \sigma_s)\omega_{ii}d\Omega - \int_\Omega f_i\omega_i d\Omega - \int_{\Gamma_f} \gamma\kappa\omega_n d\Gamma - \int_{\Gamma_c} -\xi(u_n - u_n^D)\omega_n d\Gamma - \int_{\Gamma_c} \mu\xi(u_n - u_n^D)g(\Delta\vec{u}_t)\omega_t d\Gamma = 0 \tag{22}$$

where $\omega_{ij} = (\omega_{i,j} + \omega_{j,i})/2$ and $\omega'_{ij} = \omega_{ij} - \omega_{kk}\delta_{ij}/3$.

The finite element method was used for solving eq. (22) numerically with FORTRAN. The finite element approximation on coordinate x_i and velocity $\dot{u}_i$ provided the form of matrix equations to be solved. In this simulation, axisymmetric and full three-dimensional analyses were considered with linear C_0 elements by using the implicit method for time advancement. Triangular/rectangular elements were used for axisymmetric analysis and tetrahedral/hexahedral elements were used for full three-dimensional analysis.

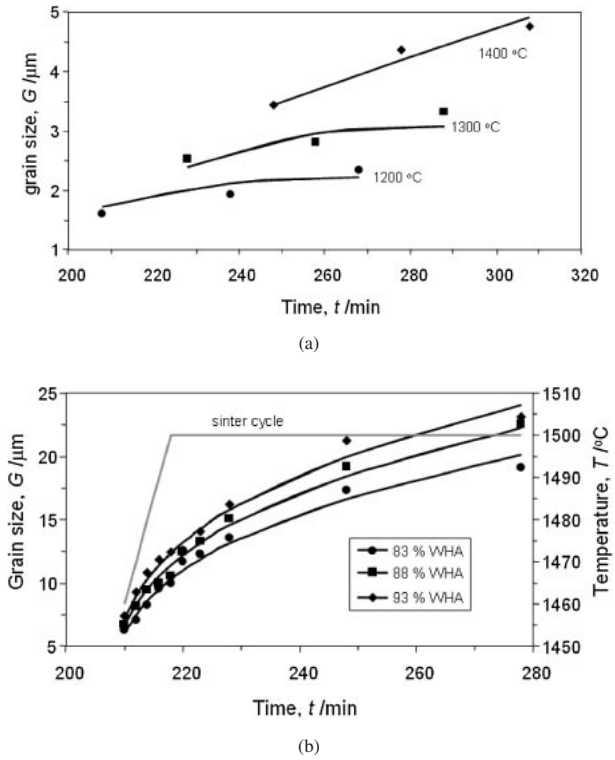

Fig. 2 Comparison of grain growth between experiment and simulation results; (a) grain growth during solid state sintering for 88% WHA and (b) grain growth during solid state sintering.

6. Results and Discussion

6.1 Grain growth

There is a three-fold increase in the grain size from approximately 1.5 to 5.5 μm during solid state sintering and a four-fold increase after liquid formation, from 5.5 μm to 20 μm. However, the rate of grain growth during solid state sintering is relatively small compared to the increase in the grain size following liquid formation. By fitting experimental grain size data based on Ostwald ripening, we found combinations of Q_G and k_0 for each composition.[21] In the solid state the apparent activation energy for grain growth (241 kJ/mol) is significantly lower than for densification (367 kJ/mol) indicating that W grain boundary diffusion is less active in grain growth than in densification. For grain growth during liquid phase sintering, the activation energy (106 kJ/mol) compares favorably with that of densification (between 101 and 136 kJ/mol), indicating that both processes proceed through a solution-reprecipitation mechanism. Figure 2 shows the comparison of experimental data and model predictions and it shows very good agreement. A sensitivity analysis shows that the sintering temperature and the activation energy for diffusion of W through the liquid are the most influential parameters that must be considered in selecting the composition or designing the sintering cycle.

6.2 Densification

In this study, a surface energy of 2.5 J/m^2 was used regardless of composition. By fitting experimental data based on the master sintering curve (MSC) concept, we found two

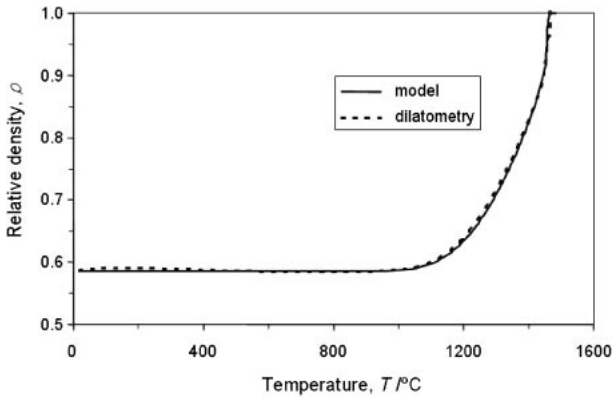

Fig. 3 Comparison of relative density versus temperature between experiment and model for 88% WHA.

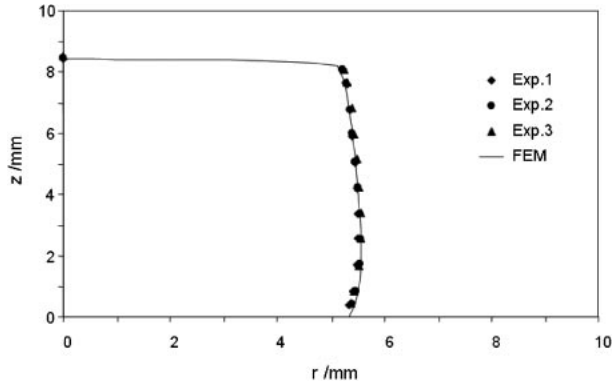

(a)

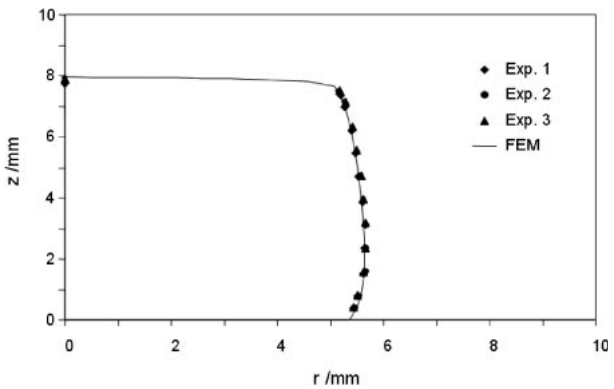

(b)

Fig. 4 Comparison of distorted shapes between experimental data and finite element simulation when the sintering temperature is 1500°C for 88% WHA; (a) 30 min hold time and (b) 60 min hold time.

combinations of Q_b and α_i for each composition.[17] Figure 3 shows the good agreement of densification behavior versus temperature between dilatometry data and model predictions for 88% WHA. For sintering of WHAs at temperatures up to 1400°C, densification occurs through a combination of both lattice diffusion of W in the additive phase and W grain boundary diffusion. At temperatures above 1455°C, solution-reprecipitation of the W particles through the Ni-Fe-W liquid phase is the dominant densification mechanism. Between 1400 and 1455°C, the MSC shows a transition region in

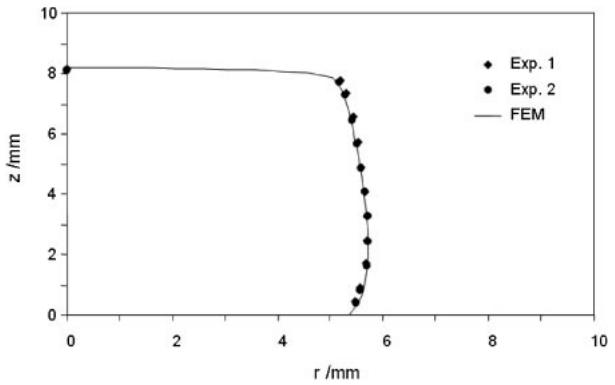

(a)

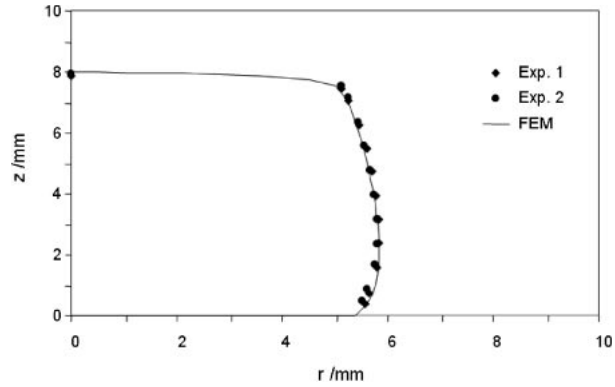

(b)

Fig. 5 Comparison of distorted shape between experimental data and finite element simulation when the sintering temperature is 1530°C for 88% WHA; (a) 30 min hold time and (b) 60 min hold time.

which a combination of the solid state and liquid phase mechanisms is active. The densification rate increases during both solid state and liquid phase sintering as the amount of W decreases.

6.3 Distortion

The amount of distortion is mainly proportional to gravity force acting on a powder compact and inversely proportional to shear viscosity. To measure shear viscosity, sinter forging or bending experiments can be used for solid state sintering. However, it is not easy to measure the material parameters for shear viscosity with the existence of liquid in a powder compact. In this study, the material parameters of the activation energy for distortion, Q_d, and the viscosity of liquid phase, η_L, were found by fitting the predicted shape by finite element method to the distorted shapes by experiment. For the finite element simulation, the analysis domain was discretized with 10×20 element meshes, representing an axi-symmetric plane from the center to the outer radius of the cylinder. As mentioned before, the relation of $\eta = 0.6K$ was used before liquid formation, that is, $T < 1455$°C.[24] The Coulomb frictional coefficient was kept constant at 0.3.

Data points in Figs. 4 and 5 show the experimentally measured distorted shapes at sintering temperatures of 1500 and 1530°C, respectively. Note the entire experiment was repeated two or three times to establish experimental accuracy. From the comparison of the distorted shapes from

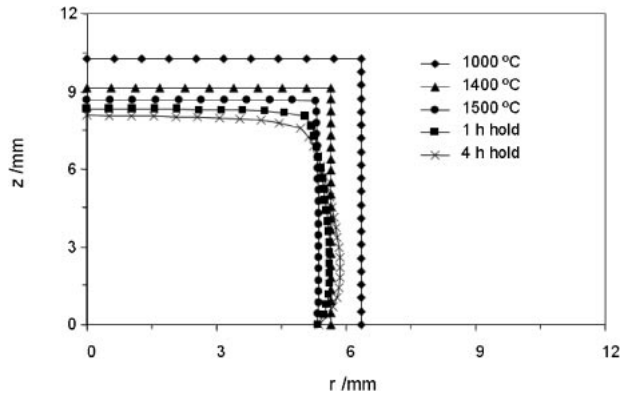

Fig. 6 Finite element simulation of densification and distortion during liquid phase sintering for 88% WHA.

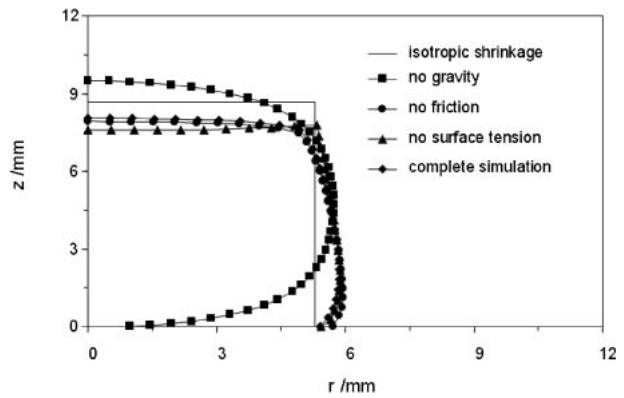

Fig. 7 Comparison of the effects of the gravity, friction, and surface tension on distortion during liquid phase sintering for 88% WHA (4 hour hold time at 1500°C).

the experiments with the finite element simulations shown in Figs. 4 and 5, the distortion behavior as well as the grain growth and the densification behavior during liquid phase sintering was precisely simulated.

Figure 6 shows the shape variations with time during liquid phase sintering. Homogeneous densification behavior was significant until full density is reached. Then, as the temperature increases, the rigidity of powder compact drops due to liquid penetration of the solid structure, resulting in distortion due to the gravity, friction, and surface tension.

To see the independent effects of gravity, friction, and surface tension on distortion, finite element simulations were carried out by numerically separating them. The analysis conditions were the same as those of distortion case explained above. A holding time of 4 hours at 1500°C was selected to magnify the amount of distortion. Figure 7 shows the individual effects of gravity, friction, and surface tension on distortion. The surface of the part is spheroidized at the corners due to the relatively high surface tension. Gravity causes slumping. Severe distortion of the part is shown at the bottom corners since friction prevented sliding of the surface in contact with the supporting plate.

Figure 8 shows the effect of the composition on distortion. Distortion increases with decreasing W content. Figure 9 demonstrates the ability of the simulation to predict distortion of three dimensional parts.

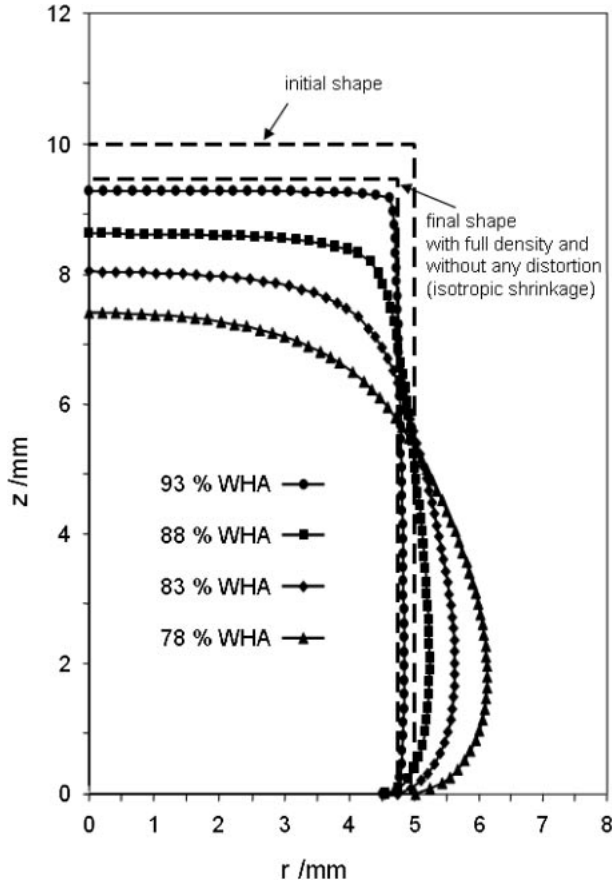

Fig. 8 Comparison of the effect of compositions on distortion during liquid phase sintering (2 hour hold time at 1500°C).

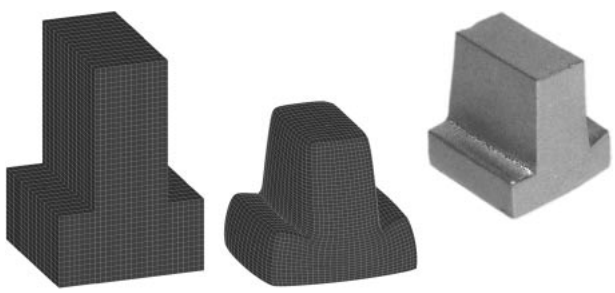

(a) T-shape

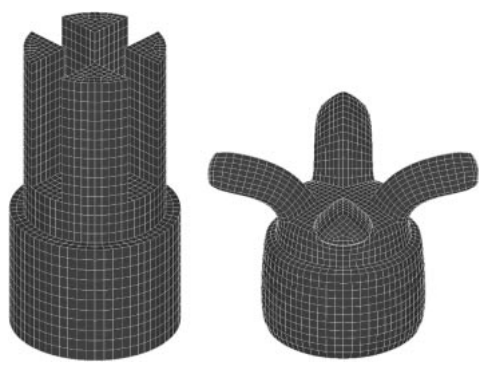

(b) cable clipper

Fig. 9 Examples of simulations of distortion of three-dimensional parts (88% WHA, 2 hour hold time at 1500°C.

7. Conclusion

The Master Sintering Curve analysis of dilatometry data can be used to determine material parameters for densification of tungsten heavy alloys before and after liquid formation. Material parameters for grain growth, which can be obtained from metallographic analysis, and material parameters for shear viscosity, which can be obtained from dimensional analysis, are also important variables in predicting densification and distortion. The use of these material parameters in constitutive equations that incorporate the bulk viscosity enables accurate modeling of densification, grain growth, and distortion during both solid state and liquid phase sintering. A finite element simulation based on these constitutive equations shows that gravity, friction, and surface tension have significant effects on densification and distortion. Gravity has the largest effect followed by surface tension and then friction. The finite element method enables prediction of distortion of three dimensional parts.

Acknowledgements

This research was supported by the National Aeronautics and Space Administration under Grant No. NAG8-1452 with Mike Purvey as Project Manager and Witold Palosz as Project Scientist. Special thanks go to Kristina Cowan for her help with the dilatometry and to Lou Campbell for his help with the metallography.

REFERENCES

1) M. F. Ashby: HIP 6.0 Background Reading and Operator Manual, Engineering Department, University of Cambridge, UK, 1990.
2) R. M. McMeeking and L. T. Kuhn: Acta Metall. Mater. **40** (1992) 961–969.
3) E. A. Olevsky, R. M. German and A. Upadhaya: Acta Mater. **48** (2000) 1167–1180.
4) H. Riedel, H. Zipse and J. Svoboda: Acta Mater. **42** (1994) 445–452.
5) P. E. McHugh and H. Riedel: Acta. Mater. **45** (1997) 2995–3003.
6) D. Bouvard and T. Meister: Modelling Simul. Mater. Sci. Eng. **8** (2000) 377–388.
7) A. C. F. Cocks: Progress in Materials Science **46** (2001) 201–229.
8) R. K. Bordia and G. W. Scherer: Acta Metall. **36** (1988) 2393–2397.
9) F. V. Lenel, H. H. Hausner, O. V. Roman and G. S. Ansell: Trans. Am. Inst. Min. Engrs. **227** (1963) 640–649.
10) A. Upadhyaya and R. M. German: Met. Mater. Trans. **29A** (1998) 2631–2638.
11) R. Raman and R. M. German: Met. Mater. Trans. **26A** (1995) 653–659.
12) R. Ganesan, A. Griffo and R. M. German: Met. Mater. Trans. **28A** (1998) 659–665.
13) C. Binet, K. L. Lencoski, D. F. Heaney and R. M. German: Met. Mater. Trans. **35A** (2004) 3833–3841.
14) A. Zavaliangos: Int. J. Powder Metall. **38** (2002) 27–39.
15) Y. S. Kwon, Y. X. Wu, P. Suri and R. M. German: Met. Mater. Trans. **35A** (2004) 257–264.
16) Y. S. Kwon and K. T. Kim: ASME J. Eng. Mat. Tech. **118** (1996) 448–455.
17) S. J. Park, J. M. Martin, J. F. Guo, J. L. Johnson and R. M. German: Metall. Mater. Trans. **37**A (2006) 2837–2848.
18) G. W. Greenwood: Acta Metall. **4** (1956) 243–248.
19) P. Lu and R. M. German: J. Mater. Sci. **36** (2001) 3385–3394.
20) V. Tikare and J. D. Cawley: Acta Mater. **46** (1998) 1343–1356.
21) S. J. Park, J. M. Martin, J. F. Guo, J. L. Johnson and R. M. German: Metall. Mater. Trans. **37**A (2006) in press.
22) A. Jagota and P. R. Dawson: J. Am. Ceram. Soc. **73** (1990) 173–177.
23) S. E. Navti, K. Ravindran, C. Taylor and R. W. Lewis: Comput. Methods Appl. Mech. Engrg. **147** (1997) 41–60.
24) P. Villars, A. Prince and H. Okamoto: *Handbook of Ternary Alloy Phase Diagrams*, vol. 8, (ASM International, 1995).